
Article:
Hafez, A. orcid.org/0000-0002-4927-1333 and Santamarina, J.C. (2024) Particle transport during asymmetric net-zero cyclic fluid flow: flow in tubes and radial flow in fractures. Powder Technology, 434. 119306. ISSN 0032-5910

https://doi.org/10.1016/j.powtec.2023.119306

Powder Technology 434 (2024) 119306

Contents lists available at ScienceDirect

Powder Technology

journal homepage: www.journals.elsevier.com/powder-technology

Particle transport during asymmetric net-zero cyclic fluid flow: Flow in tubes and radial flow in fractures

Ahmed Hafez [1,*], J. Carlos Santamarina [2]

Earth Science and Engineering, KAUST, Thuwal 23955-6900, Saudi Arabia

HIGHLIGHTS

- Asymmetric cyclic fluid flow can effectively transport insoluble particles despite net zero time-average liquid flow.
- Particle displacement can be controlled by tuning the fluid flow rates, and the fluid volume involved in each cycle.
- Asymmetric cyclic flow results in particle size segregation in both 1D and radial flow conditions.

GRAPHICAL ABSTRACT

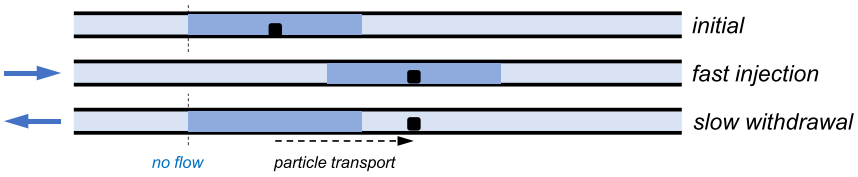

ARTICLE INFO

Keywords:
Particle-laden fluid flow
Cyclic fluid flow
Fines migration
Proppants

ABSTRACT

Cyclic fluid flow enhances transport in porous media. We study particle transport during asymmetric net-zero cyclic fluid flow where the fluid injection rate is higher than the withdrawal rate. Inside a tube, the threshold fluid velocity required to mobilize a particle depends on the relative particle size: larger particles obstruct flow more effectively than small particles and require a smaller velocity to be transported. Then, flow rates can be selected so particles move forward during the injection phase and remain stationary during withdrawal. Similarly, asymmetric cyclic fluid flow transports particles radially along fractures despite the net-zero fluid flow. The flow velocity decreases away from the injection point and particles migrate to a characteristic "terminal radial distance". Unlike tube flow, a grain has a diminishing obstructing effect on the radial flow field, and the threshold flow rate required to mobilize grains increases with increasing particle size during radial flow.

List of symbols

A [m^2]	Tube cross sectional area $A = \pi D^2/4$
Ar [ ]	Archimedes number
D [m]	Tube diameter (1D flow) or fracture aperture (radial flow)
d_p [m]	Particle diameter
F [N]	Force (F_D = drag, F_F = friction, F_S=Stokes drag, F_V = virtual mass, F_B: Basset, F_P = pressure gradient force)
m [kg]	Particle mass
N [N]	Normal force
n_{cy} [ ]	Number of cycles
P [Pa]	Fluid pressure (P_i = injection pressure, P_w = withdrawal pressure)
q [m^3/s]	Fluid flow rate (q_i = injection rate, q_w = withdrawal rate. q* = threshold flow rate for particle motion)
Re [ ]	Reynolds number
r_{max} [m]	Maximum particle radial displacement
St [ ]	Stokes number

* Corresponding author.
E-mail address: a.hafez@sheffield.ac.uk (A. Hafez).
[1] Present address: Department of Automatic Control and Systems Engineering, The University of Sheffield, UK
[2] Present address: Georgia Institute of Technology, Atlanta, USA

https://doi.org/10.1016/j.powtec.2023.119306
Received 21 August 2023; Received in revised form 5 December 2023; Accepted 18 December 2023
Available online 19 December 2023

v [m/s] Velocity (v_f = fluid velocity, v_p = particle velocity. v^* = threshold fluid velocity for particle motion)
V [m^3] Volume (V_i = injection volume, V_w = withdrawal volume, V_p = particle volume)
x_p [m] Particle position
β Substrate inclination angle
η [Pa.s] Fluid viscosity
μ [ ] Coefficient of friction
ρ [kg/m^3] Density (ρ_p = particle density, ρ_f = fluid density)
Φn [ ] Friction number

1. Introduction

Particle-laden fluid flow is ubiquitous across all scales in natural and engineered systems. Examples include blood circulation [1–3], pollen transport [4], insoluble drug delivery [5–7], proppant injection in fractures and fines transport in the subsurface [8–15]. The suspended particles experience hydrodynamic drag, inertia, self-weight, buoyancy, wall friction and electrostatic interactions [16]. Hydrodynamic forces are controlled by particle size and pore topology. For example, particles can significantly affect the fluid flow field in tubes as the particle-to-tube diameter ratio $d_p/D \rightarrow 1$; in fact, the actual drag force exceeds Stokes drag by an order of magnitude at $d_p/D = 0.6$ [17–19]. Quasi-buoyant particles ($\rho_p \approx \rho_f$) follow the fluid streamlines without deviations. However, the trajectories of both light ($\rho_p < \rho_f$) and dense particles ($\rho_p > \rho_f$) deviate from the fluid streamlines, notably in spatially varying flow fields such as in porous media [20–23].

Cyclic fluid flow enhances transport, even when the time-average liquid flux is zero: physical exercise induces cyclic stress-induced fluid flow in bones and boosts nutrient transport by enhanced mixing in lacunae pores [24–29]; periodic arterial vasodilation during sleep cycles enhances solute and waste transport in and out of the brain [30,31]; and cyclic fluid flow effectively transports heat through porous media [32].

Cyclic fluid flow can also transport insoluble particles, as observed in various natural systems. Pulsatile cardiac cycle in living organisms drives not only blood flow but also suspended components [33–35]. Respiratory cyclic flow effectively transports aerosolized drugs or dust into the lungs due to frequent particle collisions at bifurcations and the emergence of flow vortices [36–38]. Similarly, wave asymmetry and velocity skewness play a central role on sediment transport and define beach sand selection and the evolving beach morphology [39–42]; furthermore, the cyclic motion of tides and waves transports larvae into coastal inlets and fish breeding grounds, which is necessary for aquatic life [43].

The aim of this research is to study the transport of insoluble particles during asymmetric cyclic fluid flow with zero time-average liquid flow. We combine experimental, analytical and numerical methods to identify optimal transport conditions and to gain insight into underlying particle-level processes. We start with the experimental determination of the threshold fluid velocity for particle motion, which is needed to design the fluid flow cycles to cause effective particle transport. Then, we explore radial flow conditions where the velocity field decays away from the injection point. Finally, we discuss implications in different fields. Insights from this study can help understand natural processes (e.g., particle migration driven by tidal action), drug delivery methods for biological systems, and engineered geo-solutions with minimal environmental impact (e.g., proppant injection and transmissivity modification in fractures).

2. Experimental study: materials and methods

We study particle transport in tubes to identify emergent pore-scale phenomena and implications. The experimental setup consists of a transparent polyvinyl chloride PVC flexible tube (internal diameter D = 3.175 mm, length = 5.5 m) coiled into one layer of concentric circular paths. The tube outlet is submerged in a collection container placed on top of a precision scale (OHAUS Adventurer, sensitivity = 0.0001 g) connected to a computer interface to record the discharged fluid mass every second. A syringe pump (New Era NE 4000) drives the fluid flow and a pressure transducer (Omega Engineering PX209) is mounted at the tube inlet (see schematic in Fig. 1-a). The coiled tube rests horizontally and a vertically mounted camera records the test. We assess particle motion using an image-based particle tracking algorithm (see Fig. S1 for a typical particle trajectory [44,45]).

Tests involve two types of particles: cellulose acetate plastic spheres (diameter $d_p = 1$ mm, $\rho_p = 1.28$ g/cm^3, $d_p/D = 0.31$) and polypropylene plastic spheres ($d_p = 2.5$ mm $\rho_p = 0.92$ g/cm^3, $d_p/D = 0.79$). Clearly, these relatively large particles -high d_p/D ratio- affect the local flow regime in the tube; the situation resembles common conditions for particle migration in porous media.

We saturate the tube with de-aired water to prevent gas exsolution, discharge the spherical particle(s) into the tube inlet and connect the tube to the syringe pump. Then, we impose the pre-programed injection-withdrawal cycles and monitor the fluid pressure at the inlet and the discharged mass at the outlet (injection flow rate $q_i \approx 0.9$ ml/s, withdrawal flow rate $q_w = -0.005$ to -0.12 ml/s, liquid injection volume $V_i = 3.5$ ml, and withdrawal volume $V_w \approx 3.5$ ml).

3. Experimental results

3.1. Single particle in a tube

Particles move when the liquid flow rate exceeds a threshold value q^* which corresponds to a threshold flow velocity $v_f^* = q^*/A$ (average velocity for the free-tube). We determine threshold values for the 1 mm and 2.5 mm plastic spheres by running a wide range of monotonic steady state and cyclic fluid flow tests (a total of 50 tests). Fig. 2 illustrates the particle displacement after an injected volume of $V_i = 3.5$ ml. The threshold flow rate for the 1 mm sphere is $q^* \approx 0.05$ ml/s which corresponds to a free-tube average flow velocity of $v_f^* \approx 6.5$ mm/s; the corresponding threshold values for the 2.5 mm sphere are $q^* \approx 0.008$ ml/s and $v_f^* \approx 1$ mm/s. Note that contrary to particle drag in an open channel [42], the larger particle requires a smaller fluid velocity to be transported along the confined tube geometry.

The second set of experiments focuses on asymmetric cyclic flow. Fig. 3 shows data for two different asymmetric tests. The a-b-c panes on the left show a test run with $d_p = 1$ mm spherical particle using the same injection rate in all cycles $q_i = 0.9$ ml/s $> q^* = 0.05$ ml/s, but with increasing withdrawal rates in subsequent cycles: $q_w = -0.03$, -0.06, -0.09 and -0.11 ml/s. The d-e-f panes on the right of Fig. 3 show a test run with the $d_p = 2.5$ mm spherical particle using the same injection rate above the threshold value $|q_i| = 0.9$ ml/s $> q^* = 0.008$ ml/s, and a constant withdrawal rate near the threshold $|q_w| = 0.0086$ ml/s $\approx q^*$ in all cycles (see Supplementary Movie M1). The injected liquid volume in both tests V_i is equal to the withdrawn volume V_w in every cycle ($V_i = V_w = 3.5$ ml), thus the net injected liquid volume is null, V_i-$V_w = 0$ (Fig. 3-a&d).

The injection pressure $|P_i|$ is higher than the withdrawal pressure $|P_w|$ in proportion to the respective flow velocities (Fig. 3-b&e). The particle moves forward during the injection phases in both tests as $|q_i| > q^*$ (Fig. 3c&f). On the other hand, the particle backward displacement depends on the fluid withdrawal rate: it remains stationary when $|q_w| < q^*$ (1st cycle in Fig. 3c), experiences minimal return when $|q_w| \approx q^*$ (2nd cycle in Fig. 3c and all cycles in Fig. 3f), and shows significant backward displacement when $|q_w| > q^*$ (3rd and 4th cycle in Fig. 3c). The final particle displacement $\Delta x_p = 1.66$ m observed after 4 cycles in Fig. 3f approaches the average liquid displacement during injection: $n_{cy} \cdot V_i/(\pi D^2/4) = 1.74$ m. Once again, we highlight that the observed particle displacements took place with zero net fluid flow.

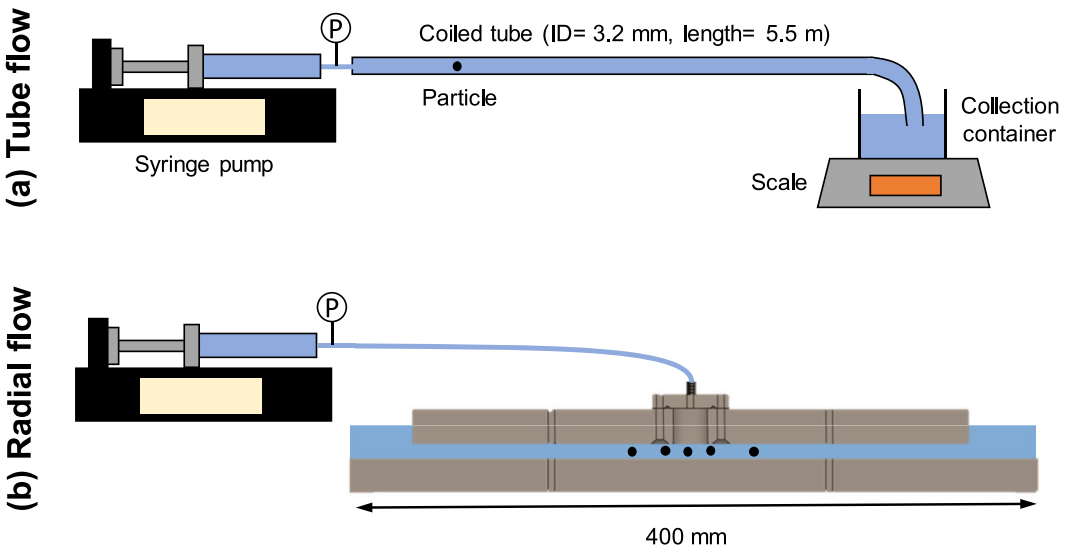

Fig. 1. Experimental setups. Devices used for (a) tube tests, and (b) radial flow tests in fractures. For clarity, the various components are sketched at different scales.

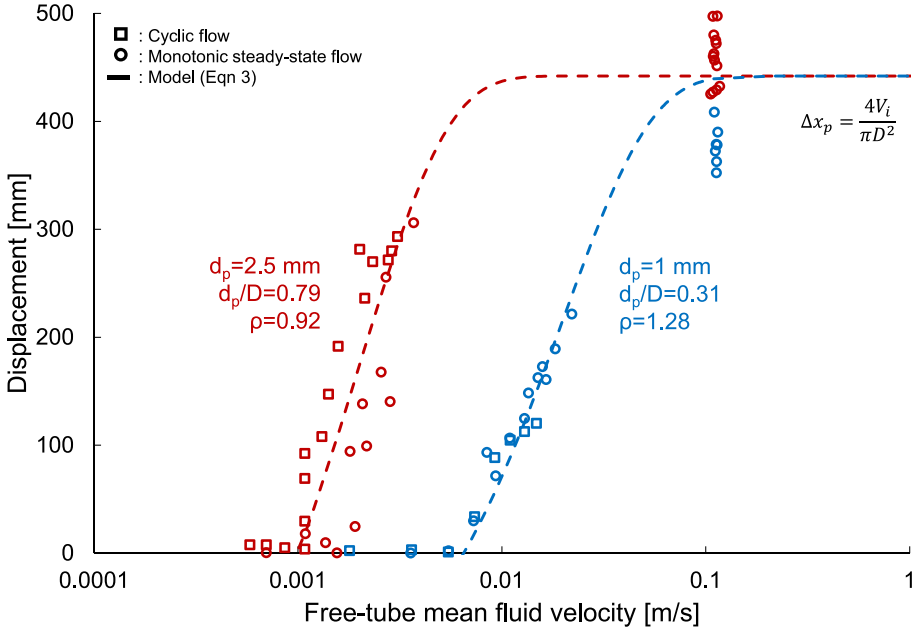

Fig. 2. Particle displacement versus free-tube mean fluid velocity (fluid injection volume $V_i = 3.5$ ml) - Threshold fluid velocity for particle transport. Tube diameter $D = 3.175$ mm. The figure includes experimental data gathered for two particle sizes $d_p = 1$ mm (blue) and $d_p = 2.5$ mm (red), under cyclic and monotonic steady-state flow. Points: experimental results. Line: fitted exponential trend (eq. 7). (For interpretation of the references to colour in this figure legend, the reader is referred to the web version of this article.)

3.2. *Multiple particles in a tube*

How do neighboring particles interact in a tube during asymmetric cyclic flow? To address this question, we run a similar set of experiments but starting with 10 small spheres closely located near the tube inlet ($d_p = 1$ mm, $d_p/D = 0.31$); then, we impose four injection-withdrawal cycles ($q_i = 0.9$ ml/s, $q_w = -0.03$ ml/s, $V_i = V_w \approx 3.5$ ml). Fig. 4-a illustrates the displacements for the ten particles; the inset shows the particle positions at the beginning and the end of the first cycle. Particles travel at different velocities, often collide as they migrate along the tube and disperse during the injection phase (see Supplementary Movie M2).

A more complex situation develops when we introduce spherical particles of different sizes. We order the particle positions such that two small spheres ($d_p = 1$ mm, $d_p/D = 0.31$) are followed by a large sphere ($d_p = 2.5$ mm, $d_p/D = 0.79$; Fig. 4-b inset). The injection-withdrawal sequence remains the same: four cycles at $q_i = 0.9$ ml/s, $q_w = -0.03$ ml/s and equal liquid volumes $V_i = V_w \approx 3.5$ ml. Results show that the three particles move together during the injection phase (Fig. 4-b). However, the withdrawal flow rate $q_w = -0.03$ ml/s is greater than the threshold rate for the large sphere ($q^* = 0.008$ ml/s) but smaller than the threshold rate for the small spheres ($q^* = 0.05$ ml/s); then, the two leading small spheres remain stationary while the large sphere moves backwards during the withdrawal phase of each cycle. Consequently, the chosen flow rates lead to particle segregation with preferential fine particle transport. We also run tests with the reverse particle sequence; in this case, the finer particles remain trapped behind the larger particle.

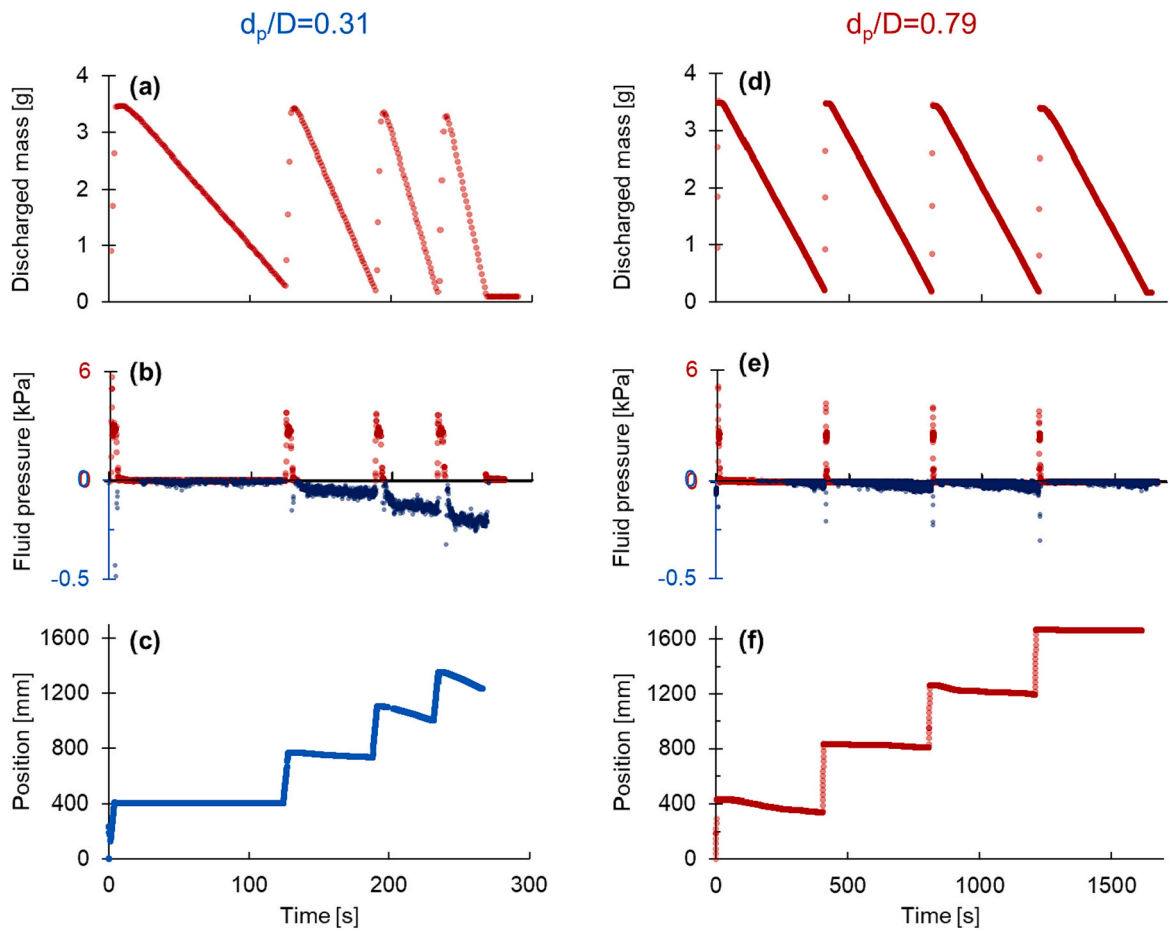

Fig. 3. Single particle transport in a tube during cyclic fluid flow. Left: (a) discharged liquid mass, (b) fluid pressure and (c) particle position (estimated using image-based particle tracking) as a function of time for a 1 mm spherical particle: $d_p/D = 0.31$, $\rho_p = 1.28$ g/cm^3. Right: (d) discharged liquid mass, (e) fluid pressure and (f) particle position as a function of time for a 2.5 mm spherical particle; $d_p/D = 0.79$, $\rho_p = 0.92$ g/cm^3.

4. Analyses and discussion

4.1. Particle motion in a tube

A stationary particle subjected to transient fluid flow within a confined tube experiences forces related to hydrodynamic drag F_D, the fluid pressure difference across the particle F_P and friction against walls F_F. As the flow velocity increases beyond the threshold velocity, the particle accelerates (inertial force) and affects the surrounding fluid which contributes to a virtual fluid mass force F_V that retards particle motion [46]; in addition, the delay in boundary layer development during changes in relative velocity adds "history" and the transient Basset force F_B. Then, the equation of motion (horizontal x-direction) for the particle flowing in a tube is [16,47]:

$$\rho_p V_p \frac{d^2 x_p}{dt^2} = F_D + F_p - F_F - F_V + F_B \tag{1}$$

The particle detaches from the wall at high flow velocities [48–50], the friction force vanishes and all other forces acting on the particle change in response to the evolving particle position within the tube.

4.2. Dimensionless ratios

The governing forces combine to define the governing dimensionless ratios in terms of the particle and tube diameters d_p and D, particle and fluid mass densities ρ_p and ρ_f, fluid viscosity η and flow velocity v_f [23,51]:

$$\text{Fluid Reynolds number } Re = \frac{\text{Inertial force}}{\text{Viscous force}} = \frac{\rho_f v_f D}{\eta} \tag{2}$$

$$\text{Stokes number } St = \frac{\text{Particle response time}}{\text{Fluid response time}} = \frac{\rho_p d_p^2 v_f}{18\,\eta\,D} \tag{3}$$

$$\text{Friction number } \Phi n = \frac{\text{Viscous drag force}}{\text{Friction force}} = \frac{6\,F_D}{\pi\, d_p^3 (\rho_p - \rho_f)\, g\, |\cos\beta|\, \mu} \tag{4}$$

$$\text{Archimedes number } Ar = \frac{\text{Particle weight}}{\text{Viscous force}} = \frac{g\, d_p^3 \rho_f\, (\rho_p - \rho_f)}{\eta^2} \tag{5}$$

where the substrate inclination β, acceleration due to gravity g and the friction coefficient μ define the frictional resistance. The values of Reynolds number *Re* computed for the fluid in the tube without an obstruction are:

- small sphere ($d_p = 1$ mm): $Re \approx 360$ during injection and $5 < Re < 70$ during withdrawal
- large sphere ($d_p = 2.5$ mm): $Re \approx 360$ during injection and $1 < Re < 12$ during withdrawal

The inertial forces are significant during fluid injection ($Re >> 1$) and the creeping flow approximation to the Navier-Stokes equation becomes inaccurate during the injection phase [52]. (Note: the validation simulations in Fig. S2-a show that the creeping flow approximation, including Hagan Poiseuille flow, is valid for most of the *Re* values

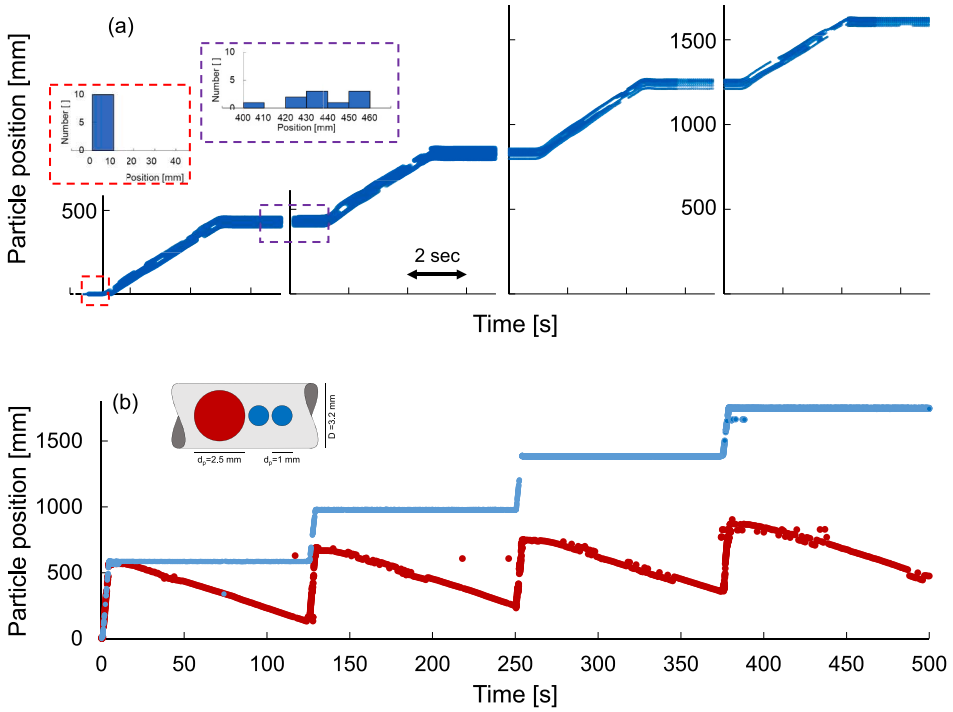

Fig. 4. Transport of multiple particles in a tube during asymmetric cyclic fluid flow. (a) Mono-size spheres: 10 small spherical particles ($d_p = 1$ mm, $d_p/D = 0.31$, $D = 3.175$ mm). Inset: particle positions at the beginning and end of the first cycle – see Supplementary Movie M2. (b) Dual size spheres: two small spheres (blue, $d_p = 1$ mm) followed by one large sphere (red, $d_p = 2.5$ mm) - See inset. Injection-withdrawal sequence: 4 cycles, $q_i = 0.9$ ml/s, $q_w = -0.03$ ml/s, $V_i = V_w \approx 3.5$ ml. (For interpretation of the references to colour in this figure legend, the reader is referred to the web version of this article.)

imposed during fluid withdrawal). Particles with large Stokes numbers maintain their trajectories due to inertia and resist changes in motion [23]. In our experiments, $St < 1$, thus the particles largely follow the fluid streamlines during flow. In addition, $Ar >> 1$ due to the low water viscosity and particles initially migrate towards the tube wall by gravity. During high flow rate injection, particles displace inwards away from the walls due to lift forces, Segré-Silberberg effect or turbulence [48–50]. Particle displacement starts when $\Phi n > 1$.

4.3. Analytical approximation

Given the different concurrent processes and transient effects, there is no closed-form analytical solution for the particle motion in a tube at high *Re* and large d_p/D ratios. We can obtain a first-order closed-form solution for the particle displacement by disregarding the virtual mass and history effects, and assuming Stokes law to approximate the drag force $F_S = 3\pi\eta d_p(v_p - v_f)$. (Note: this assumption applies for low $Re < 1$ and small size ratio $d_p/D < 0.1$; [50,53,54]:

$$\text{Displacement}: x_p(t) - x_p(0) = \left(\frac{4q}{\pi D^2} - \frac{\mu N}{3\pi\eta d_p}\right) * \left(\frac{m}{3\pi\eta d_p} e^{\frac{-3\pi\eta d_p t}{m}} - \frac{m}{3\pi\eta d_p} + t\right) \tag{6}$$

Inspired by this expression, we fit an exponential trend to the experimental data compiled in Fig. 2, where we adopt two asymptotic values: (1) the liquid displacement estimated with the average flow velocity $\Delta x_p = v_f\, t = V_i/(\pi D^2/4)$ and (2) null particle displacement when the mean fluid flow velocity is below the threshold value $v_f < v^*$:

$$\Delta x_p = \begin{cases} \dfrac{4V_i}{\pi D^2}\left(1 - e^{\lambda\,(v^* - v_f)}\right) & \text{if } v_f > v^* \\ 0 & \text{if } v_f < v^* \end{cases} \tag{7}$$

where the exponential decay rate λ is a fitting parameter ($\lambda = 500$ s/mm for the large sphere, and $\lambda = 50$ s/mm for the small sphere). Note that the maximum particle motion can exceed the value estimated using the average flow velocity v_f: quasi-buoyant ($\rho_p \approx \rho_f$) small ($d_p/D \to 0$) particles migrate along the tube centerline with velocity $v_{max} = 2{\cdot}v_f$ (parabolic velocity profile - Hagen–Poiseuille).

4.4. Numerical simulations

We use COMSOL Multiphysics to investigate the threshold flow rate q^* and mean flow velocity v_f^* when the particle is at the verge of motion $v_p = 0$, thus eq. 1 becomes $F_D + F_P = F_F$. The simulation solves the Navier-Stokes equation using finite element simulations (No-slip boundary conditions along the cylinder walls). The 3D simulation domain consists of a water-filled cylinder that mimics the tube used in our experiments (internal diameter $D = 3.175$ mm; length = 30 mm). Simulation results provide the fluid pressure and velocity field around the particle; then, we compute F_D and F_P by integrating the fluid shear stress and pressure acting against the sphere (see the supplementary information and Fig. S2-S3 for more details).

We compare numerical predictions for different flow rates q and experimental results to estimate the static friction coefficient μ for the small and large particles (made of different materials). At the onset of particle displacement, the computed friction coefficients are: $\mu = 0.11$ for the small cellulose acetate sphere ($v_f^* = 6.5$ mm/s) and $\mu = 0.18$ for the large polypropylene particle ($v_f^* = 1$ mm/s). Previous studies report a friction coefficient $\mu = 0.21$ for a polypropylene sphere rolling against an acrylic sheet [55]. This result offers a first-order verification of our simulations.

Previous analytical and numerical studies report the ratio between the actual drag force F_D and the Stokes drag F_S as a wall correction factor: $F_D/F_S = 2.2$ for $d_p/D = 0.3$ and $F_D/F_S = 40$-to-70 for $d_p/D = 0.8$ when $Re < 1$ [17–19,56]. We run complementary numerical simulations for the geometry corresponding to our experimental study (the particle fixed at the center of the cylinder and the average flow velocity is $v_f = 6.3$ mm/s). Fig. 5 shows that the pressure drop and the drag force acting on the particle increase as the relative particle size d_p/D increases and the cross-sectional area for fluid flow decreases; the trend follows an

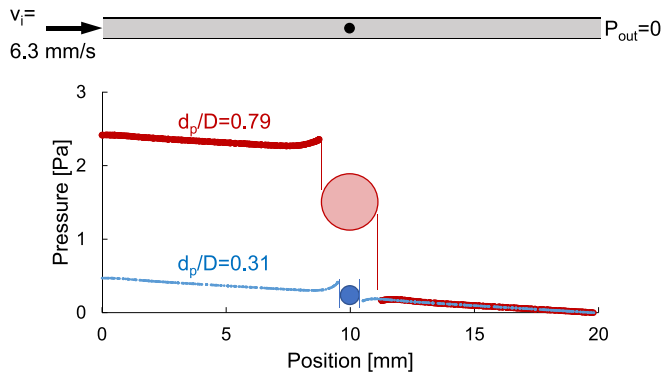

Fig. 5. Obstructed fluid flow in tubes: effects on fluid pressure – Numerical simulation. The stationary spherical particle is fixed at the center of the cylindrical tube. Pressure along the tube centerline for two particle diameters: d_p = 2.5 mm (red, d_p/D = 0.79) and d_p = 1 mm (blue, d_p/D = 0.31). Tube diameter D = 3.175 mm. Imposed flow velocity v_i = 6.3 mm/s. Outlet pressure P_{out} = 0. (For interpretation of the references to colour in this figure legend, the reader is referred to the web version of this article.)

inverse power relation (Fig. S4):

$$\frac{F_D}{F_s} = \frac{1}{\left(1 - d_p/D\right)^{2.5}} \tag{8}$$

This trend converges to the Stokes drag regime for small particles in large tubes: $F_D/F_S \to 1$ as $d_p/D \to 0$. The force caused by the pressure drop across the particle gains relevance as the relative particle size increases $d_p/D > 0$, and $F_D/F_S \to \infty$ when the particle blocks the tube $d_p/D \to 1$ (Fig. S4).

The friction number $\Phi n = F_D/F_F$, i.e., the ratio between viscous drag within a tube and frictional resistance (eq. 4) can now be related to Stokes viscous drag in an infinite volume $F_S = 3\pi\eta d_p(v_p\text{-}v_f)$ by combining eqs. 4 and 8:

$$\Phi n = \frac{F_D}{F_F} = \frac{F_s}{F_F} * \frac{1}{\left(1 - d_p/D\right)^{2.5}} = \frac{18\eta v_f}{d_p^2 g\left(\rho_p - \rho_f\right)\mu\cos\beta} * \frac{1}{\left(1 - d_p/D\right)^{2.5}} \tag{9}$$

Fig. S5 shows that particle displacement data collapse onto a single trend when plotted in terms of the dimensionless friction number Φn (Note: we use μ-values estimated from the simulations above - Fig. S3. For completeness, Fig. S5 shows the same analytical model (eq. 7) applied to the dataset with λ = 0.4). Once again, the threshold friction number is $\Phi n = 1$ at the onset of particle movement.

Finally, we investigate the fluid flow field around five identical spherical particles inside the tube during the injection phase. We impose an injection flow rate q_i = 0.9 ml/s equal to the experiments (fluid velocity v_i = 114 mm/s, d_p = 1 mm, center-to-center distance = 1.6 mm, d_p/D = 0.31). The first and last particles in the sequence experience higher shear stress and drag forces than the intermediate particles (See figure in supplementary information - Fig. S3-c). Thus, the last particle in the direction of fluid flow (particle 5 in Fig. S3-c) moves faster and collides with its immediate neighbor. In turn, this particle accelerates (conservation of momentum) and collides with the next one, and so on. Therefore, particles travel at different velocities, and often collide and disperse during fluid injection, as experimentally observed in this study (see Fig. 4-a inset and Supplementary Movie M2).

4.5. Radial flow

The flow velocity in isotropic radial flow decreases inversely proportional to the radial distance to the injection point. What are the implications for asymmetric cyclic flow and particle transport? We investigate this question using two transparent parallel acrylic disks separated at a constant gap to mimic a fracture (disk diameter = 400 mm, gap height or aperture D = 1.45 mm. Schematic diagram in Fig. 1-b. Similar device as in [57]). A flexible tube connects the parallel-plates to a syringe pump and we discharge 10 g of silica sand into the central tube at the beginning of each cycle (silica sand, 75 μm < d_p < 250 μm, 0.05 < d_p/D < 0.17).

Fig. 6 illustrates sand migration during six injection-withdrawal cycles (q_i = 4 ml/s, q_w = −1.6 ml/s, V_i = V_w = 82 ml – See Supplementary Movie M3). Similar to tube flow, radial asymmetric cyclic fluid flow transports sand particles along the gap between the plates, despite the zero time-average injected volume, V_i-V_w = 0. As the flow velocity decreases away from the injection point, particles will migrate to a characteristic "terminal radial distance". In this study, the sand particles migrated to r_{max} = 0.13 m at the end of the 6th cycle. We combine Stokes drag force and Coulomb friction to obtain a first-order estimate of the terminal radial migration distance (Note: this assumption applies for low *Re* < 1 and small size ratio d_p/D < 0.1):

$$r_{max} = \frac{9}{\pi}\frac{\eta\, q}{d_p^2 D\left(\rho_p - \rho_f\right) g\mu} \tag{10}$$

For parameters relevant to this experiment, the estimated terminal radial migration distance is r_{max} = 0.13 m when the sand-wall friction is μ = 0.37 (ρ_f = 1000 kg/m^3, ρ_p = 2650 kg/m^3, mean diameter d_p = 0.1 mm, viscosity η = 0.001 Pa.s, imposed flow rate q = 4 ml/s, and fracture gap D = 1.45 mm).

Unlike the tube configuration, the presence of a grain has a diminishing obstructing effect on the flow field between two plates, and the threshold flow rate q* required to mobilize grains increases with increasing particle size during radial particle-laden fluid flow (see results in [42]). The coarse particles remain stationary during fluid withdrawal, since $q_w < q^*$, while finer particles retreat to the inlet (notice the retreat of fine particles in Supplementary Movie M3). Thus, asymmetric cyclic radial flow in fractures can be engineered to cause the preferential migration of coarse particles, contrary to confined particle migration in a tube.

Sand grains injected at the beginning of a new injection cycle gradually catch up with sand injected in previous cycles; together they form an annular ring around the inlet that alters the pressure field. Successive erosion-infilling can be observed under various flow conditions; this sequence of events may displace the final location of the ring beyond the single particle terminal distance r_{max} (eq. 10).

5. Implications

The energy geoengineering field makes extensive use of hydraulic fracturing to create a network of interconnected pathways in the subsurface that facilitate fluid flow and resource recovery (Gas recovery: [58–63]. Deep geothermal heat recovery: [64–67]). Particles are injected to prop fractures open and to install granular filters [68–71]. This is a water intensive procedure that demands 10-to-50 million liters of water per well and involves dozens of chemicals [72–74]; >70% of the injected water remains in the subsurface and chemical additives can contaminate groundwater resources [73].

Clearly, particle transport driven by asymmetric cyclic fluid flow with net-zero fluid injection can minimize water demand and mitigate the negative environmental effects associated to well stimulation: operators inject the sand slurry at a high flow rate and withdraw water at a low flow rate so the sand remains in position. The injected and withdrawn water volumes are equal, i.e., V_i-V_w = 0. The water recovered at the end of one cycle is reused in the subsequent cycles.

In the medical field, heart failure is one of the leading causes of hospitalization and death [75–77]. Due to the shortage of available organ donors, artificial heart pumps have emerged as viable options. Heart pumps are either volume-displacement pumps that deliver pulsatile blood flow [78] or more compact continuous-flow pumps [79]. However, continuous flow pumps are associated with complications

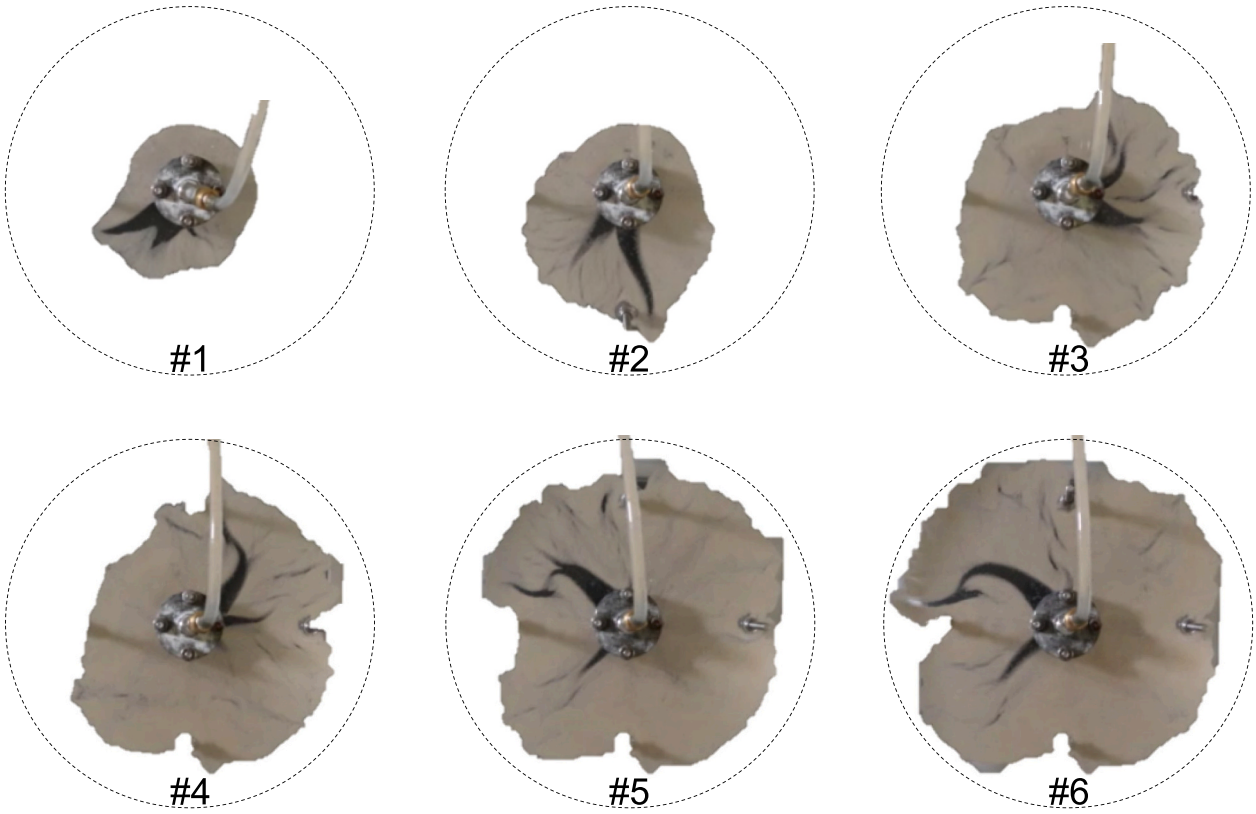

Fig. 6. Particle transport in a fracture plane driven by asymmetric cyclic radial flow. Silica sand added at the beginning of each cycle (10 g per cycle). Dotted circle: 265 mm diameter. Particles: 75 μm < d_p < 250 μm. Water injection and withdrawal rates: $q_i = 4$ ml/s and $q_w = -1.6$ ml/s. Gap aperture D = 1.45 mm. Disk diameter: 400 mm. $V_i = V_w = 82$ ml. Images show sand migration at the end of each cycle. Setup in Fig. 1-b. See also Supplementary Movie M3.

such as blood clots, vessel stiffening and blood hemolysis probably due to the lack of pulsation [33]. Thus, current research efforts aim to re-introduce pulsatile fluid flow through pump speed modulation [33,79].

6. Conclusions

This study explored particle transport during asymmetric cyclic fluid flow with net-zero time average flux. The combined experimental-numerical investigation focused on confined tube flow and included implications to radial flow. Salient conclusions follow:

- Asymmetric cyclic fluid flow can effectively transport insoluble particles despite net zero time-average liquid flow.
- Particle displacement depends on the competition between hydrodynamic drag, friction and inertial forces. Therefore, particle displacement can be controlled by tuning the injection and withdrawal flow rates, and the fluid volume involved in each cycle.
- The threshold flow rate or fluid velocity required to mobilize a particle depends on the relative particle size. Thus, cyclic fluid flow promotes particle size segregation.
- Larger particles obstruct flow more effectively in a tube and cause a higher pressure drop; hence larger particles, i.e., higher d_p/D ratio, exhibit a lower threshold velocity for mobilization. Consequently, coarse particles may retreat during fluid withdrawal in a tube, while fine particles remain stationary.
- The opposite situation is observed in radial flow such as in fractures and unconfined flow: higher flow velocities are needed to mobilize larger particles. As the flow velocity is inversely proportional to radial distance, a characteristic terminal distance for particle transport emerges in radial flow.

Supplementary data to this article can be found online at https://doi.org/10.1016/j.powtec.2023.119306.

Funding

This work was supported by the King Abdullah University of Science and Technology KAUST Endowment.

Contributions

Both authors contributed substantially to the manuscript and approved the final submission.

CRediT authorship contribution statement

Ahmed Hafez: Data curation, Formal analysis, Investigation, Methodology, Software, Validation, Visualization, Writing – original draft. **J. Carlos Santamarina:** Conceptualization, Formal analysis, Funding acquisition, Investigation, Methodology, Project administration, Resources, Supervision, Writing – review & editing.

Declaration of Competing Interest

The authors declare that they have no known competing financial interests or personal relationships that could have appeared to influence

the work reported in this paper.

Data availability

All data generated or analyzed during this study are included in this published article (and its Supplementary Information files).

Acknowledgements

This work was conducted by the authors while at King Abdullah University of Science and Technology KAUST. Gabrielle E Abelskamp edited the manuscript.

References

[1] L. Schramm, Introduction, Emulsions, Foams, Suspensions, and Aerosols, 2014, pp. 1–22.
[2] A. Marin, H. Lhuissier, M. Rossi, C.J. Kähler, Clogging in constricted suspension flows, Phys. Rev. E 97 (2018), 021102.
[3] S. Ma, X. Qi, K. Han, S. Wang, G. Hu, X. Li, Computational investigation of flow dynamics and mechanical retention of age-associated red blood cells in the spleen, Phys. Rev. Fluids 8 (2023), 063103.
[4] M. Sofiev, J. Belmonte, R. Gehrig, R. Izquierdo, M. Smith, Å. Dahl, P. Siljamo, Airborne pollen transport, Allergenic pollen (2013) 127–159.
[5] S. Kalepu, V. Nekkanti, Insoluble drug delivery strategies: review of recent advances and business prospects, Acta Pharm. Sin. B 5 (2015) 442–453.
[6] R.J. Kuhn, Pharmaceutical considerations in aerosol drug delivery, Pharmacother. J. Human Pharmacol. Drug Therapy 22 (2002) 80S–85S.
[7] Y. Li, O. Amili, F. Coletti, Experimental study of concentrated particle transport in successively bifurcating vessels, Phys. Rev. Fluids 7 (2022), 083101.
[8] S. Tong, K.K. Mohanty, Proppant transport study in fractures with intersections, Fuel 181 (2016) 463–477.
[9] Y. Liu, M.M. Sharma, Effect of fracture width and fluid rheology on proppant settling and retardation: An experimental study, in: SPE Annual Technical Conference and Exhibition, Society of Petroleum Engineers, Dallas, Texas, 2005, p. 12.
[10] K.S. Novakowski, P.A. Lapcevic, Field measurement of radial solute transport in fractured rock, Water Resour. Res. 30 (1994) 37–44.
[11] J.P. Herzig, D.M. Leclerc, P.L. Goff, Flow of suspensions through porous media—application to deep filtration, Ind. Eng. Chem. 62 (1970) 8–35.
[12] H.S. Fogler, K. Khilar, Migrations of Fines in Porous Media, Springer, 1998.
[13] M. Vahab, N. Khalili, An X-FEM formulation for the optimized graded proppant injection into hydro-fractures within saturated porous media, Transp. Porous Media 121 (2018) 289–314.
[14] P. Bedrikovetsky, N. Caruso, Analytical model for fines migration during water injection, Transp. Porous Media 101 (2014) 161–189.
[15] H. Qu, S. Tang, Z. Liu, J. McLennan, R. Wang, Experimental investigation of proppant particles transport in a tortuous fracture, Powder Technol. 382 (2021) 95–106.
[16] C.T. Crowe, J.D. Schwarzkopf, M. Sommerfeld, Y. Tsuji, Multiphase Flows with Droplets and Particles, CRC Press, 2011.
[17] S. Krishnan, A. Kaman, Effect of blockage ratio on drag and heat transfer from a centrally located sphere in pipe flow, Eng. Appl. Comput. Fluid Mech. 4 (2010) 396–414.
[18] J. Happel, H. Brenner, Wall Effects on the Motion of a Single Particle, Low Reynolds Number Hydrodynamics: With Special Applications to Particulate Media, Springer, Netherlands, Dordrecht, 1983, pp. 286–357.
[19] P.L. Paine, P. Scherr, Drag coefficients for the movement of rigid spheres through liquid-filled cylindrical pores, Biophys. J. 15 (1975) 1087–1091.
[20] J.R. Valdes, J.C. Santamarina, Particle clogging in radial flow: microscale mechanisms, SPE-88819-PA 11 (2006) 193–198.
[21] J.R. Valdes, J.C. Santamarina, Particle transport in a nonuniform flow field: retardation and clogging, Appl. Phys. Lett. 90 (2007), 244101.
[22] G. Kampel, G.H. Goldsztein, J.C. Santamarina, Particle transport in porous media: the role of inertial effects and path tortuosity in the velocity of the particles, Appl. Phys. Lett. 95 (2009), 194103.
[23] Q. Liu, B. Zhao, J.C. Santamarina, Particle migration and clogging in porous media: a convergent flow microfluidics study, J. Geophys. Res. Solid Earth 124 (2019) 9495–9504.
[24] K. Piekarski, M. Munro, Transport mechanism operating between blood supply and osteocytes in long bones, Nature 269 (1977) 80–82.
[25] L. Wang, S.C. Cowin, S. Weinbaum, S.P. Fritton, Modeling tracer transport in an osteon under cyclic loading, Ann. Biomed. Eng. 28 (2000) 1200–1209.
[26] G.H. Goldsztein, J.C. Santamarina, Solute transport during cyclic flow in saturated porous media, Appl. Phys. Lett. 85 (2004) 2432–2434.
[27] J.J. Claria, G.H. Goldsztein, J.C. Santamarina, A.C. Diffusion, Transport in porous networks subjected to zero-time-average advective flow, Transp. Porous Media 93 (2012) 51–61.
[28] S.C. Cowin, Bone poroelasticity, J. Biomech. 32 (1999) 217–238.
[29] M.L. Knothe Tate, Mixing mechanisms and net solute transport in bone, Ann. Biomed. Eng. 29 (2001) 810–811.
[30] L. Bojarskaite, D.M. Bjørnstad, A. Vallet, K.M.G. Binder, C. Cunen, K. Heuser, M. Kuchta, K.-A. Mardal, R. Enger, Sleep cycle-dependent vascular dynamics enhance perivascular cerebrospinal fluid flow and solute transport, bioRxiv, 2022, 2022.2007.2014.500017.
[31] D.H. Kelley, Brain cerebrospinal fluid flow, Phys. Rev. Fluids 6 (2021), 070501.
[32] T.S. Yun, B. Dumas, J.C. Santamarina, Heat transport in granular materials during cyclic fluid flow, Granul. Matter 13 (2011) 29–37.
[33] N. Moazami, W.P. Dembitsky, R. Adamson, R.J. Steffen, E.G. Soltesz, R.C. Starling, K. Fukamachi, Does pulsatility matter in the era of continuous-flow blood pumps? J. Heart Lung Transplant. 34 (2015) 999–1004.
[34] N. Takeishi, M.E. Rosti, Enhanced axial migration of a deformable capsule in pulsatile channel flows, Phys. Rev. Fluids 8 (2023) L061101.
[35] A. Tiwari, S.S. Chauhan, Effect of varying viscosity on two-layer model of pulsatile flow through blood vessels with porous region near walls, Transp. Porous Media 129 (2019) 721–741.
[36] C. Kleinstreuer, Z. Zhang, Z. Li, Modeling airflow and particle transport/deposition in pulmonary airways, Respir. Physiol. Neurobiol. 163 (2008) 128–138.
[37] J.L. Gurman, M. Lippmann, R.B. Schlesinger, Particle deposition in replicate casts of the human upper tracheobronchial tree under constant and cyclic inspiratory flow. I. Experimental, Aerosol Sci. Technol. 3 (1984) 245–252.
[38] C.S. Kim, L. Garcia, Particle deposition in cyclic bifurcating tube flow, Aerosol Sci. Technol. 14 (1991) 302–315.
[39] H.A. Einstein, Sediment transport by wave action, Coast. Eng. 1972 (1972) 933–952.
[40] S. Elgar, E.L. Gallagher, R.T. Guza, Nearshore sandbar migration, J. Geophys. Res. Oceans 106 (2001) 11623–11627.
[41] F. Grasso, H. Michallet, E. Barthélemy, Sediment transport associated with morphological beach changes forced by irregular asymmetric, skewed waves, J. Geophys. Res. Oceans 116 (2011).
[42] L. Zuo, D. Roelvink, Y. Lu, S. Li, On incipient motion of silt-sand under combined action of waves and currents, Appl. Ocean Res. 69 (2017) 116–125.
[43] C.A. Brown, G.A. Jackson, D.A. Brooks, Particle transport through a narrow tidal inlet due to tidal forcing and implications for larval transport, J. Geophys. Res. Oceans 105 (2000) 24141–24156.
[44] D.H. Kelley, N.T. Ouellette, Using particle tracking to measure flow instabilities in an undergraduate laboratory experiment, Am. J. Phys. 79 (2011) 267–273.
[45] J. Schindelin, I. Arganda-Carreras, E. Frise, V. Kaynig, M. Longair, T. Pietzsch, S. Preibisch, C. Rueden, S. Saalfeld, B. Schmid, J.-Y. Tinevez, D.J. White, V. Hartenstein, K. Eliceiri, P. Tomancak, A. Cardona, Fiji: an open-source platform for biological-image analysis, Nat. Methods 9 (2012) 676–682.
[46] Z.-S. Mao, C. Yang, Numerical evaluation of virtual mass force coefficient of single solid particles in acceleration, Chin. J. Chem. Eng. 41 (2022) 210–219.
[47] M.R. Maxey, J.J. Riley, Equation of motion for a small rigid sphere in a nonuniform flow, the, Phys. Fluids 26 (1983) 883–889.
[48] S.Z. Ali, S. Dey, Bed particle saltation in turbulent wall-shear flow: a review, Proc. Roy. Soc. A Math. Physical Eng. Sci. 475 (2019) 20180824.
[49] G. Segré, A. Silberberg, Radial particle displacements in Poiseuille flow of suspensions, Nature 189 (1961) 209–210.
[50] D. Fjaestad, I. Tomac, Experimental investigation of sand proppant particles flow and transport regimes through narrow slots, Powder Technol. 343 (2019) 495–511.
[51] A. Hafez, Q. Liu, J.C. Santamarina, Magneto-rheological fluids: tele-manipulation of ferromagnetic particles with external magnetic field for flow control and zonal isolation, Geoenergy Sci. Eng. 228 (2023), 212029.
[52] S.H. Lee, K.-K. Lee, I.W. Yeo, Assessment of the validity of Stokes and Reynolds equations for fluid flow through a rough-walled fracture with flow imaging, Geophys. Res. Lett. 41 (2014) 4578–4585.
[53] X. Guan, X. Li, N. Yang, M. Liu, CFD simulation of gas-liquid flow in stirred tanks: effect of drag models, Chem. Eng. J. 386 (2020), 121554.
[54] A.H. Sulaymon, C.A.M.E. Wilson, A.I. Alwared, Experimental determination of the virtual mass coefficient for two spheres accelerating in a power law fluid, J. Fluids Eng. 132 (2010).
[55] S. Alborzi, D. Abrahamyan, S.M. Hashmi, Mixing particle softness in a two-dimensional hopper: particle rigidity and friction enable variable arch geometry to cause clogging, Phys. Rev. E 107 (2023), 024901.
[56] R.M. Wham, O.A. Basaran, C.H. Byers, Wall effects on flow past solid spheres at finite Reynolds number, Ind. Eng. Chem. Res. 35 (1996) 864–874.
[57] A. Hafez, Q. Liu, T. Finkbeiner, T.E. Moellendick, J.C. Santamarina, Rapid bentonite-cement-oil hydration: implications to fluid loss control, J. Pet. Sci. Eng. 215 (2022), 110615.
[58] D. Zhang, P.G. Ranjith, M.S.A. Perera, The brittleness indices used in rock mechanics and their application in shale hydraulic fracturing: a review, J. Pet. Sci. Eng. 143 (2016) 158–170.
[59] T. Guo, S. Zhang, Z. Qu, T. Zhou, Y. Xiao, J. Gao, Experimental study of hydraulic fracturing for shale by stimulated reservoir volume, Fuel 128 (2014) 373–380.
[60] M.J. Economides, D.N. Mikhailov, V.N. Nikolaevskiy, On the problem of fluid leakoff during hydraulic fracturing, Transp. Porous Media 67 (2007) 487–499.
[61] D. Li, S. You, Q. Liao, M. Sheng, S. Tian, Prediction of shale gas production by hydraulic fracturing in Changning area using machine learning algorithms, Transp. Porous Media 149 (2023) 373–388.
[62] D. Wang, S. Li, D. Zhang, Z. Pan, Understanding and predicting proppant bedload transport in hydraulic fracture via numerical simulation, Powder Technol. 417 (2023), 118232.
[63] K.M.A.S. Bandara, P.G. Ranjith, T.D. Rathnaweera, Improved understanding of proppant embedment behavior under reservoir conditions: a review study, Powder Technol. 352 (2019) 170–192.

[64] D.B. Fox, D.L. Koch, J.W. Tester, The effect of spatial aperture variations on the thermal performance of discretely fractured geothermal reservoirs, Geothermal Energy 3 (2015) 21.
[65] B. Gee, R. Gracie, M.B. Dusseault, Multiscale short-circuiting mechanisms in multiple fracture enhanced geothermal systems, Geothermics 94 (2021), 102094.
[66] P. Li, J. Zheng, B. Dou, H. Tian, H. Liu, P. Xiao, J. Chen, A 3-D numerical simulation-based heat production performance research for enhanced geothermal system with two horizontal wells and rectangular multiparallel fractures, Num. Heat Transf. B: Fundamentals (2021) 1–24.
[67] M. AbuAisha, B. Loret, Stabilization of forced heat convection: applications to enhanced geothermal systems (EGS), Transp. Porous Media 112 (2016) 229–252.
[68] R.J. Saucier, Considerations in gravel pack design, J. Pet. Technol. 26 (1974) 205–212.
[69] J.V.M. de Magalhães, A. Calderon, A.L. Martins, Gravel-pack-placement limits in extended horizontal offshore Wells, SPE Drill. Complet. 21 (2006) 193–199.
[70] A.L. Martins, J.V.M. de Magalhães, A. Calderon, C.M. Chagas, A mechanistic model for horizontal gravel-pack displacement, SPE-88819-PA 10 (2005) 229–237.
[71] M. Roostaei, O. Kotb, M. Mahmoudi, V. Fattahpour, C. Wang, A. Nouri, B. Fermaniuk, An Experimental Investigation into Gravel Pack Performance in Steam-Drive Operations, SPE Western Regional Meeting, 2018.
[72] J. Backstrom, in: T.C.F.G.A. Opportunity (Ed.) (Ed.), Strategic Reporting and the Effects of Water Use in Hydraulic Fracturing on Local Groundwater Levels in Texas, Utah State University, 2019.
[73] I. Oraki Kohshour, T. Leshchyshyn, J. Munro, M.C. Yorro, A.T. Adejumo, U. Ahmed, R. Barati, I. Kugler, M. Reynolds, M. Cullen, J. McAndrew, D. Wedel, Examination of Water Management Challenges and Solutions in Shale Resource Development - Could Waterless Fracturing Technologies Work?, SPE/AAPG/SEG Unconventional Resources Technology Conference, 2016.
[74] M. Cook, K.L. Huber, M.E. Webber, Who regulates it? Water policy and hydraulic fracturing in Texas, Texas Water J. 6 (2015) 45–63.
[75] V.L. Roger, Epidemiology of heart failure, Circ. Res. 113 (2013) 646–659.
[76] A. Groenewegen, F.H. Rutten, A. Mosterd, A.W. Hoes, Epidemiology of heart failure, Eur. J. Heart Fail. 22 (2020) 1342–1356.
[77] M. Cowie, A. Mosterd, D. Wood, J. Deckers, P. Poole-Wilson, G. Sutton, D. Grobbee, The epidemiology of heart failure, Eur. Heart J. 18 (1997) 208–225.
[78] I. Gosev, M.S. Kiernan, P. Eckman, B. Soleimani, A. Kilic, N. Uriel, J.D. Rich, J. N. Katz, J. Cowger, B. Lima, S. McGurk, M.A. Brisco-Bacik, S. Lee, S.M. Joseph, C. B. Patel, Long-term survival in patients receiving a continuous-flow left ventricular assist device, Ann. Thorac. Surg. 105 (2018) 696–701.
[79] D. Mancini, P.C. Colombo, Left ventricular assist devices: a rapidly evolving alternative to transplant, J. Am. Coll. Cardiol. 65 (2015) 2542–2555.